

1 The role of dust mineral composition in atmospheric radiation and pollution in North 2 China: new insights from EMIT and two-way coupled modeling

3
4 Chao Gao¹, Xuelei Zhang^{1,2,*}, Hu Yang¹, Ling Huang³, Hongmei Zhao¹, Shichun Zhang¹, and Aijun Xiu¹

5
6 ¹State Key Laboratory of Black Soils Conservation and Utilization, Northeast Institute of Geography and Agroecology,
7 Chinese Academy of Sciences, Changchun, 130102, China

8 ²School of Geographical Sciences, Liaoning Normal University, Dalian, 116029, China

9 ³School of Environmental and Chemical Engineering, Shanghai University, Shanghai 200444, China

10 *Correspondence to: X.L. Zhang (zhangxuelei@neigae.ac.cn)

11 12 Abstract

13 Mineral dust is a major atmospheric aerosol influencing Earth's energy balance
14 through aerosol–radiation (ARI) and aerosol–cloud interactions (ACI). While
15 homogeneous dust effects have been studied, the impact of mineralogical composition on
16 regional meteorology and air quality remains underexplored, limiting accurate forecasting
17 of dust storm impacts, especially in dust belt regions. In this study, we used a two-way
18 coupled WRF-CHIMERE model with three mineralogical dust atlases (Nickovic et al.
19 (2012) (N2012), Journet et al. (2014) (J2014), and a new dataset, Li et al. (2024) (L2024),
20 from the Earth Surface Mineral Dust Source Investigation (EMIT)) to evaluate ARI effects
21 during the March 2021 dust storm in North China. Results showed significant spatial
22 variations in radiative forcing due to mineralogical differences. Bulk dust (without
23 considering mineralogy) caused an average shortwave radiative forcing of -5.72 W m^{-2} ,
24 while mineral-specific forcings increased this by up to $+0.10 \text{ W m}^{-2}$. Integrating EMIT
25 data reduced PM_{10} biases by over 15% in high-concentration regions and improved ozone
26 predictions, with localized changes of -2.46 to $+3.52 \mu\text{g m}^{-3}$. Hematite's strong absorption
27 and quartz's reflective properties were key in altering radiative and air quality outcomes.
28 Compared to scenarios of bulk dust, the consideration of ARI effects of mineralogical
29 compositions can increase PM_{10} concentration by up to $1189.48 \mu\text{g m}^{-3}$ in dust source
30 regions. Future research perspectives on the utilization of high-resolution EMIT data in
31 two-way coupled meteorology and air quality models for investigating the ACI effects of

32 mineralogical dust on cloud microphysics are proposed.

33 **1 Introduction**

34 Mineral dust, a dominant component of global atmospheric aerosols, primarily
35 originates from wind erosion in arid and semi-arid regions (Schepanski, 2018; Shao et al.,
36 2011). It can affect the Earth's energy balance through direct scattering and absorption of
37 solar, i.e. aerosol–radiation interaction (ARI), as well as indirect effects on cloud properties
38 by acting as cloud condensation nuclei and ice nuclei, i.e., aerosol–cloud interaction (ACI)
39 (Chooari et al., 2014; Kok et al., 2023). By altering biogeochemical cycles, atmospheric
40 chemistry and visibility, and air quality, transported mineral dust can exacerbate economic
41 losses, and health risks (Adebiyi et al., 2023; Cwiertny et al., 2008; Duniway et al., 2019;
42 Maher et al., 2010; Tong et al., 2023). Accurate forecasting of mineral dust events is crucial
43 to mitigate these adverse impacts.

44 Numerous studies have demonstrated that the magnitude of dust ARI and ACI effects
45 is significantly influenced by its mineralogical composition. For instance, iron oxides,
46 particularly hematite and goethite, have been identified as key components responsible for
47 dust absorption of solar radiation, as evidenced by both observational and modeling studies
48 (Alfaro et al., 2004; Gómez Maqueo Anaya et al., 2024; Lafon et al., 2006; Li et al., 2022;
49 Obiso et al., 2024; Scanza et al., 2015; Song et al., 2024). Concurrently, a growing body of
50 research has explored the impact of various dust mineral compositions, including hematite,
51 corundum, kaolinite, mica, montmorillonite, quartz, calcite, illite, amorphous silicon,
52 aluminum silicate, and potassium feldspar, on ice nucleation processes. Among these,
53 potassium feldspar has emerged as a crucial component for dust nucleation activation
54 (Harrison et al., 2016; Kumar et al., 2018). However, a notable gap exists in our
55 understanding of how specific mineral compositions impact meteorology and air quality
56 through ARI and ACI effects. Prior research has predominantly focused on homogeneous
57 dust aerosols, assuming globally uniform composition and optical properties. However,
58 this assumption introduces regional inaccuracies in estimating the impacts of dust aerosols,

59 which remain poorly understood due to uncertainties in dust composition (Ke et al., 2022;
60 Klingmüller et al., 2019; Kok et al., 2017).

61 Many efforts have been directed to improve simulations of dust mineralogy and its
62 representation in numerical models (Balkanski et al., 2021; Gómez Maqueo Anaya et al.,
63 2024; Gonçalves Ageitos et al., 2023; Li et al., 2021, 2022, 2024; Li and Sokolik, 2018;
64 Menut et al., 2020; Obiso et al., 2024; Scanza et al., 2015; Solomos et al., 2023b, a; Song
65 et al., 2024). Most of the above are offline models, with only two studies conducting two-
66 way feedback simulations with only WRF-Chem (Li and Sokolik, 2018) and WRF-
67 CHIMERE (Menut et al., 2020) being applied. However, both of these studies are derived
68 from artificially generated data and lack effective ground-based validation, as discussed in
69 Claquin et al. (1999), Nickovic et al. (2012) (N2012 hereafter), and Journet et al. (2014)
70 (J2014 hereafter). These validations predominantly focus on agricultural regions rather
71 than the arid and semi-arid areas that are major sources of dust emissions (Green et al.,
72 2020). EMIT instrument provides a new approach to invert and obtain the surface soil
73 mineral composition and further assess the ARI and ACI effects of dust minerals (Connelly
74 et al., 2021). To the best of our knowledge, no prior research has investigated the impact
75 of dust on regional meteorology and air quality while considering its mineral speciation
76 using two-way coupled models with three different mineralogical dust atlases.

77 Since the aerosol nucleation processes (ACI effects) of specific mineral components
78 are not represented in the current two-way coupled WRF-CHIMERE framework, the
79 present study concentrates on the ARI effects of dust minerals. This focus ensures a clear
80 and robust assessment of how mineralogical composition influences radiative processes,
81 without introducing additional uncertainties arising from incomplete cloud-related
82 parameterizations. In this study, we employ a two-way coupled WRF-CHIMERE model
83 with three mineralogical databases to investigate how dust composition influences
84 radiation and meteorology in North China during a severe dust storm. Section 2 describes
85 the model configuration and data sources, Section 3 presents the simulations with emphasis

86 on ARI-induced impacts on meteorology and air quality, and Section 4 summarizes the
87 main findings.

88

89 **2 Methodology and data**

90 **2.1 Model configurations and data sources**

91 The two-way coupled WRF model version 3.7.1 and CHIMERE model version
92 2020r3 were employed to simulate the ARI and ACI effects of mineralogical dust particles
93 on meteorology and air quality over North China from March 12 to March 15, 2021. The
94 exchanges between meteorological and air quality variables are accomplished through the
95 OASIS coupler (Briant et al., 2017). The simulation was conducted at a horizontal
96 resolution of 27 km, with 165 grid cells in the east-west direction and 87 in the north-south
97 direction, and the study domain is depicted in Fig. S1. The model has 33 vertical levels
98 from surface to 50 hPa with 13 layers in the bottom 1 km and the bottom thickness being
99 24.5 m. The Rapid Radiative Transfer Model for General circulation models (RRTMG)
100 shortwave and longwave radiation schemes were employed to investigate the ARI effects
101 (Briant et al., 2017). Additionally, the Thompson cloud microphysics scheme was utilized
102 to assess the impacts of ACI (Tuccella et al., 2019). The initial and boundary conditions
103 (ICs and BCs) for non-dust aerosols are prescribed by the LDMZ-INCA model, while those
104 for dust aerosols are determined by the GOCART model. The options of other physics and
105 chemistry schemes are presented in Table S1. The dry depositions are treated as described
106 in Zhang et al. (2001). The parameterizations for the removal of dust particles below clouds
107 by raindrops and snow are based on the methods proposed by Willis & Tattelman (1989)
108 and Wang et al. (2014), respectively. Inline mineral dust emissions, incorporating
109 mineralogy, are computed using a u^* threshold and a dust production model for saltation
110 (Kok et al., 2014; Shao and Lu, 2000). The model accounts for the impact of soil moisture
111 on suppressing mineral dust emissions (Fécan et al., 1998). To minimize meteorological
112 bias, a spectral nudging approach is applied (Menut et al., 2024).

113 For the calculations of ARI effects in WRF-CHIMERE, refractive indices

114 corresponding to these mineralogical species are provided in Table 2 of Menut et al. (2020).
115 Concerning shortwave (SW) radiation, the aerosol optical properties, encompassing single
116 scattering albedos and asymmetry factors at 400 and 600 nm, as well as the aerosol optical
117 depth (AOD) at 300, 400, and 999 nm, calculated using Fast-JX, were interpolated or
118 extrapolated to obtain values at 14 SW intervals (Briant et al., 2017; Gao et al., 2022). AOD
119 at 16 longwave (LW) intervals ranging from 3400 to 55600 nm are directly used to
120 calculate LW radiation.

121 To evaluate the performance of the WRF-CHIMERE model with and without
122 mineralogical dust emissions, we compiled a comprehensive set of environmental
123 observations, as shown in Fig. S1. Hourly PM₁₀ and O₃ concentrations (132 observations)
124 were obtained from <https://quotsoft.net/air/>, which aggregates official monitoring data
125 from the Ministry of Ecology and Environmental Protection of China. Shortwave radiation
126 (SSR) data (59 hourly measurements) were obtained from Tang et al. (2019), with the
127 original measurements sourced from the China Meteorological Administration. Hourly
128 surface meteorological data (844 observations) were also obtained from the China
129 Meteorological Administration (<https://data.cma.cn>). All datasets were subjected to quality
130 control procedures, including checks for outliers, unit consistency, and temporal alignment,
131 to ensure reliability and integrity.

132

133 **2.2 Mineral dust atlases**

134 Accurate soil composition data are essential for partitioning dust emission fluxes into
135 contributions from individual minerals. Mineral density and refractive index data were
136 obtained from Menut et al. (2020). Three global mineralogical composition datasets
137 (N2012, J2014, and EMIT) provide information on 12 mineral species (Table 1) at different
138 spatial resolutions (1 km × 1 km and 0.5° × 0.5°).

139 To ensure a consistent spatial framework and facilitate cross-dataset integration, the
140 N2012 dataset (originally provided at 1 km × 1 km resolution and available at
141 <http://www.seevccc.rs/GMINER30>) was resampled to 0.5° × 0.5°. The J2014 dataset,

142 widely employed in the WRF–CHIMERE modeling framework, includes 12 mineral
143 species distributed across the clay and/or silt fractions (see Table 2 in Menut et al., 2020).
144 In contrast, the EMIT dataset (<https://earth.jpl.nasa.gov/emit/data/data-products>) required
145 additional preprocessing, as it reports only normalized spectral abundances rather than
146 mineral mass fractions. These spectral abundances were therefore recalculated to represent
147 the normalized mass proportions of each mineral in each substrate. Furthermore, EMIT
148 does not include data for feldspar and quartz, necessitating additional correction procedures
149 described below.

150 When the total mineral composition from EMIT summed to less than 100%, indicating
151 missing mineral contributions, the residual fraction was assigned to quartz and feldspar
152 based on their relative proportions in J2014 or N2012. Because EMIT reports illite and
153 mica as a single category, their individual abundances were separated according to the
154 ratios found in N2012 or J2014. For minerals that occur in both clay and silt fractions,
155 EMIT values were partitioned following the relative contributions from N2012 or J2014.

156 For minerals not directly observed by EMIT (e.g., quartz and feldspar), their mass
157 fractions were estimated using soil-type conversion methods from previous studies
158 (Claquin et al., 1999; Journet et al., 2014). The spatial distributions of clay and silt were
159 obtained from the global SoilW texture dataset
160 (<http://globalchange.bnu.edu.cn/research/soilw>) at 1 km resolution and resampled to 0.5°
161 to match EMIT data. Similarly, the J2014 and N2012 mineral datasets were resampled to
162 0.5° resolution. Major minerals extracted from EMIT L3 include calcite, dolomite, chlorite,
163 goethite, gypsum, hematite, illite+mica, kaolinite, montmorillonite, and vermiculite.
164 Notably, in the official EMIT L3B dataset (https://data.lpdaac.earthdatacloud.nasa.gov/lp-prod-protected/EMITL3ASA.001/EMIT_L3_ASA_001/EMIT_L3_ASA_001.nc), illite
165 and mica are combined because they were jointly identified during the Tetracorder analysis
166 of L2B data using mineral groups 1 and 2 and the corresponding band depths
167 of L2B data using mineral groups 1 and 2 and the corresponding band depths
168 (<https://github.com/nasa/EMIT-Data->

169 Resources/blob/main/data/mineral_grouping_matrix_20230503.csv).

170 The EMIT mineral fractions were normalized so that their sum at each grid point did
171 not exceed unity. Any remaining fraction was attributed to quartz and feldspars according
172 to their relative proportions in J2014 or N2012. To ensure consistency with the CHIMERE
173 mineral representation, dolomite was merged into calcite, illite+mica was separated into
174 illite and mica, and montmorillonite was treated as smectite. The mineral fractions were
175 then converted to density-weighted values and renormalized at each grid point so that the
176 total sum equaled one. Finally, each mineral was partitioned into clay and silt fractions
177 based on the J2014 ratios, and the resulting fractions were normalized using Equations (1)–
178 (4). The processed dataset was exported as a NetCDF file to serve as input for the
179 CHIMERE model.

180 To ensure mineral mass balance and model consistency, a normalization and
181 partitioning procedure was applied as follows. Equation (1) defines the total mass fraction
182 (MF_j) of mineral j as the sum of its contributions from the clay (MFC_j) and silt (MFS_j)
183 fractions:

$$184 \quad MF_j = MFC_j + MFS_j \text{ for all } j \in M_{\text{CHIMERE}} \quad (1)$$

185 Equation (2) enforces a normalization constraint so that the sum of all mineral mass
186 fractions equals unity at each grid point.

$$187 \quad 1 = \sum_{j \in M_{\text{CHIMERE}}} MF_j \quad (2)$$

188 The normalized total fraction of each mineral (MF_j^*) was then redistributed between
189 clay and silt according to their relative contributions in the reference dataset (J2014 or
190 N2012), as shown in Equations (3) and (4):

$$191 \quad MFS_j^* = MF_j^* \frac{MFS_j}{MFS_j + MFC_j} \quad (3)$$

$$192 \quad MFC_j^* = MF_j^* \frac{MFC_j}{MFS_j + MFC_j} \quad (4)$$

193 Here, MFS_j^* and MFC_j^* represent the normalized mass fractions of mineral j in the

194 silt and clay fractions, respectively. The weighting terms MFS_j and MFC_j preserve the
 195 clay–silt distribution patterns derived from the reference datasets while maintaining the
 196 normalized total (MF_j^*).

197 Table 1. Mineralogical compositions in different datasets.

| Mineral | Clay | | Silt | | EMIT |
|-------------|-------|-------|-------|-------|----------------|
| | N2012 | J2014 | N2012 | J2014 | |
| Smectite | ✓ | ✓ | ✗ | ✗ | ✓ |
| Illite | ✓ | ✓ | ✗ | ✗ | ✓ [†] |
| Hematite | ✓ | ✓ | ✓ | ✗ | ✓ |
| Feldspar | ✗ | ✓ | ✓ | ✓ | ✗ |
| Kaolinite | ✓ | ✓ | ✗ | ✗ | ✓ |
| Calcite | ✓ | ✓ | ✓ | ✓ | ✓ |
| Quartz | ✓ | ✓ | ✓ | ✓ | ✗ |
| Gypsum | ✗ | ✗ | ✓ | ✓ | ✓ |
| Vermiculite | ✗ | ✓ | ✗ | ✗ | ✓ |
| Chlorite | ✗ | ✓ | ✗ | ✓ | ✓ |
| Goethite | ✗ | ✗ | ✗ | ✓ | ✓ |
| Mica | ✗ | ✗ | ✗ | ✓ | ✓ [†] |
| Resolution | 1 km | 0.5° | 1 km | 0.5° | 0.5° |

198 [†] indicates the content of illite + mica

199

200 2.3 Scenario set up

201 Ten parallel WRF-CHIMERE simulations were performed to investigate the influence
 202 of mineralogical dust on meteorology and air quality in China, employing three distinct
 203 mineralogical atlases, as illustrated in Figs. 1 and S5-S7. Each simulation was conducted
 204 both with and without enabling ARI effects, as detailed in Table 2, to isolate and compare
 205 the effects of mineralogical dust under different modeling conditions.

206 Simulations without ARI effects (Dust_NO, N2012_Default_NO, N2012_EMIT_NO,
 207 J2014_Default_NO, J2014_EMIT_NO) were specifically designed to identify the direct
 208 impact of mineralogical dust on meteorology and air quality, independent of the radiative

209 feedbacks induced by aerosols. These No_ARI simulations served as a baseline for
 210 assessing how mineralogical compositions affect meteorology and air quality in the
 211 absence of aerosol–radiation feedback mechanisms.

212 In contrast, simulations with ARI enabled (Dust_ARI, N2012_Default_ARI,
 213 N2012_EMIT_ARI, J2014_Default_ARI, J2014_EMIT_ARI) were used to quantify the
 214 additional effects arising from aerosol–radiation interactions. By comparing simulations
 215 with and without ARI for each mineralogical atlas (e.g., N2012_Default_ARI –
 216 N2012_Default_NO), the differential impact of ARI effects on meteorology and air quality
 217 for various dust compositions could be identified. This approach highlights how
 218 mineralogical properties of dust influence the strength and nature of ARI effects, thereby
 219 modulating key atmospheric processes such as radiation balance, temperature profiles, and
 220 pollutant distributions.

221 To evaluate the discrepancies in ARI effects among the mineralogical atlases,
 222 differences in the ARI impacts between EMIT-derived and default dust compositions were
 223 analyzed for both N2012 and J2014 datasets. For example, comparisons such as
 224 (N2012_EMIT_ARI – N2012_EMIT_NO) versus (N2012_Default_ARI –
 225 N2012_Default_NO) provide insight into the extent to which higher-resolution, satellite-
 226 derived mineralogical data influence ARI effects relative to default atlas-based
 227 representations. Similar comparisons were performed for the J2014 dataset.

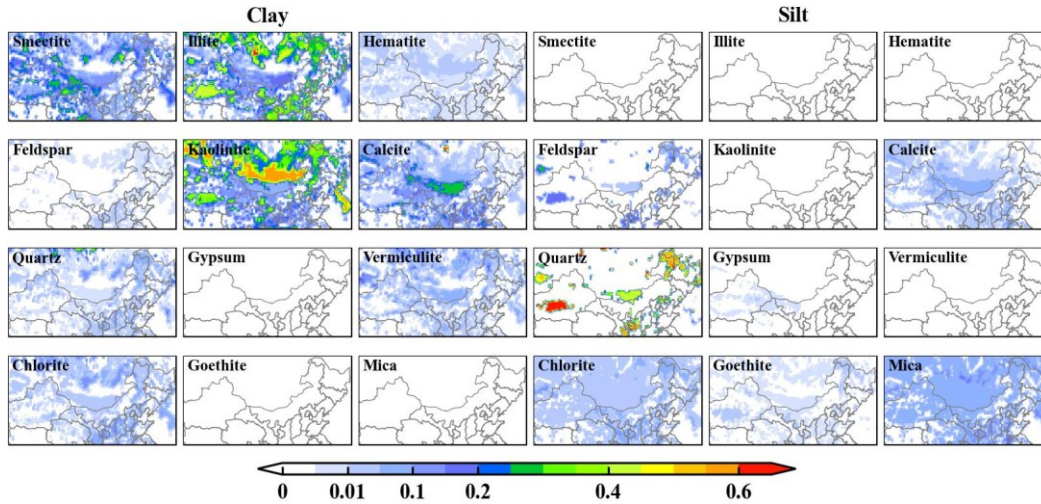
228

229 Table 2. Summary of dust emission scenarios and aerosol feedback configurations for
 230 different simulation settings.

| Scenario | Emission | Online | Coupling type | Aerosol feedback |
|-------------------|--|--------------|----------------|------------------|
| Dust_NO | Bulk dust + anthropogenic emissions | [online] = 1 | [cpl_case] = 1 | No feedbacks |
| Dust_ARI | | [online] = 1 | [cpl_case] = 2 | ARI effects |
| N2012_Default_NO | N2012_Default dust + anthropogenic emissions | [online] = 1 | [cpl_case] = 1 | No feedbacks |
| N2012_Default_ARI | | [online] = 1 | [cpl_case] = 2 | ARI effects |
| N2012_EMIT_NO | N2012_EMIT dust + anthropogenic emissions | [online] = 1 | [cpl_case] = 1 | No feedbacks |
| N2012_EMIT_ARI | | [online] = 1 | [cpl_case] = 2 | ARI effects |
| J2014_Default_NO | J2014_Default dust + anthropogenic emissions | [online] = 1 | [cpl_case] = 1 | No feedbacks |

| | | | | |
|-------------------|---------------------------------|--------------|----------------|--------------|
| J2014_Default_ARI | emissions | [online] = 1 | [cpl_case] = 2 | ARI effects |
| J2014_EMIT_NO | J2014_EMIT dust + anthropogenic | [online] = 1 | [cpl_case] = 1 | No feedbacks |
| J2014_EMIT_ARI | emissions | [online] = 1 | [cpl_case] = 2 | ARI effects |

231



232

233 Figure 1. Spatial distribution of content for the different mineral dust species in the silt and clay fraction
 234 of the soil for original J2014 mineralogical data.

235

236 3 Results and discussion

237 3.1 Evaluation of meteorology and air quality

238 Table 3 presents the evaluation results for observed and simulated surface shortwave
 239 radiation (SSR), 2-meter temperature (T2), and 10-meter wind speed (WS10) from various
 240 scenario simulations conducted using the WRF-CHIMERE modeling system. The model
 241 demonstrates strong overall performance, with correlation coefficients (R) between
 242 observed and simulated values reaching approximately 0.7 for SSR and WS10, and up to
 243 0.93 for T2. These results indicate the model's ability to capture key atmospheric patterns
 244 and variability across the simulation domain. Nevertheless, systematic biases are apparent,
 245 particularly in North China, where the model tends to overestimate SSR and WS10 by
 246 60.69%–68.92% and 17.06%–17.52%, respectively, while underestimating T2 by 0.48%–
 247 0.58%. The overestimation of SSR likely results from uncertainties in cloud development
 248 associated with planetary boundary layer and convection parameterizations (Alapaty et al.,
 249 2012). The systematic overestimation of 10-m wind speed under low-wind conditions

250 commonly observed in weather models mainly stems from outdated geographic data and
251 coarse spatial resolution (Gao et al., 2024).

252 A comparative analysis of the two configurations, N2012 and J2014, reveals that
253 WRF-CHIMERE with N2012 generally outperforms J2014 in simulating SSR and T2,
254 suggesting that the N2012 parameterization better captures radiative and thermodynamic
255 processes in the region. Conversely, J2014 exhibits improved accuracy in simulating WS10,
256 implying potential strengths in its representation of near-surface wind dynamics. These
257 findings highlight the sensitivity of model performance to parameterization schemes and
258 the need for tailored configurations for specific meteorological variables. The inclusion of
259 detailed dust mineralogical compositions, while informative for certain applications,
260 introduces additional complexities that reduce the overall accuracy of simulations.
261 Specifically, while these compositions help mitigate the overestimation of SSR and the
262 underestimation of T2, they exacerbate the overestimation of WS10. The integration of
263 EMIT satellite data provides a significant boost to model performance, highlighting the
264 value of incorporating high-resolution, real-time observational data to refine the simulation
265 of atmospheric variables. EMIT data, with its detailed characterization of aerosol and dust
266 properties, reduces the positive biases in SSR and WS10 while simultaneously minimizing
267 the negative biases in T2.

268 When comparing the ARI effects of the defaulted mineralogical compositions in
269 N2012 and J2014 with simulations that implement EMIT satellite data, the latter shows a
270 clear advantage. Incorporating EMIT data further reduces the positive biases in SSR and
271 WS10, while simultaneously minimizing the negative biases in T2. This suggests that
272 EMIT data provides a more precise representation of dust properties and atmospheric
273 conditions, enhancing the overall reliability of the model.

274

275 Table 3. Statistics analysis of daily averaged SSR, 2-meter temperature (T2) and 10-meter wind speed
276 (WS10) from different scenario simulations and ground observations in North China including
277 correlation coefficient (R) and normalized mean bias (NMB).

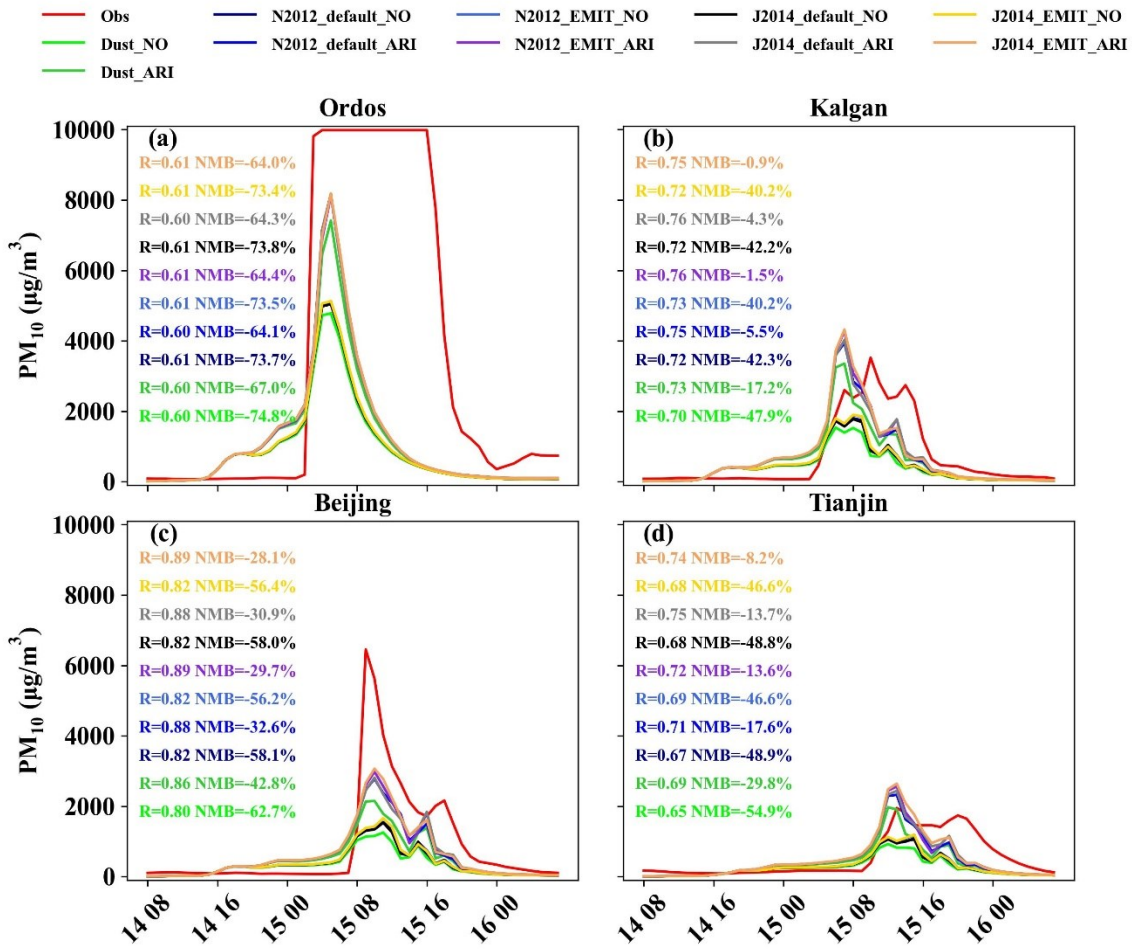
| Scenario | SSR | T2 | WS10 |
|----------|-----|----|------|
|----------|-----|----|------|

| | R | NMB (%) | R | NMB (%) | R | NMB (%) |
|-------------------|------|---------|------|---------|------|---------|
| Dust_NO | 0.70 | 68.92 | 0.93 | -0.58 | 0.71 | 17.06 |
| Dust_ARI | 0.72 | 60.69 | 0.94 | -0.48 | 0.72 | 17.46 |
| N2012_Default_NO | 0.70 | 68.92 | 0.93 | -0.58 | 0.71 | 17.06 |
| N2012_Default_ARI | 0.71 | 61.80 | 0.94 | -0.48 | 0.72 | 17.53 |
| N2012_EMIT_NO | 0.70 | 68.92 | 0.93 | -0.58 | 0.71 | 17.06 |
| N2012_EMIT_ARI | 0.72 | 60.88 | 0.94 | -0.48 | 0.72 | 17.44 |
| J2014_Default_NO | 0.70 | 68.92 | 0.93 | -0.58 | 0.71 | 17.06 |
| J2014_Default_ARI | 0.71 | 61.68 | 0.94 | -0.48 | 0.72 | 17.51 |
| J2014_EMIT_NO | 0.70 | 68.92 | 0.93 | -0.58 | 0.71 | 17.06 |
| J2014_EMIT_ARI | 0.72 | 61.22 | 0.94 | -0.48 | 0.72 | 17.48 |

278

279 To assess the ability of each scenario simulation to replicate regional PM₁₀ and O₃
280 temporal patterns, Figure 2 presents hourly time series of simulated and in situ PM₁₀ and
281 O₃ concentrations at four North China sites: Ordos, Kalgan, Beijing, and Tianjin. These
282 locations represent key dust aerosol transport pathways, which play a crucial role in the
283 region's air quality dynamics due to frequent dust storms and anthropogenic emissions.
284 The time series plots regarding PM₁₀ and O₃ in Figures 2 and S2 allow for a direct
285 comparison of model simulations with observed data, revealing important insights into
286 model performance across different environmental conditions and geographical settings,
287 respectively. The models exhibit relatively high correlations for PM₁₀, with R values
288 ranging from 0.61 to 0.89 and NMBs from -73.8% to -0.9%. In contrast, their performance
289 for O₃ is notably weaker, with R values between 0.25 and 0.63 and NMBs from +10.9% to
290 +84.2%. Among the simulations, N2012 with EMIT data and ARI effects provides the best
291 performance for PM₁₀, while N2012 with EMIT data without aerosol effects performs best
292 for O₃ concentrations. All models accurately captured the peak PM₁₀ and O₃ concentrations
293 observed during the March 12 event in North China, which was characterized by significant
294 dust emissions and high pollutant levels. This event serves as a key test case for evaluating
295 the models' responsiveness to extreme atmospheric conditions. However, despite the
296 overall agreement in peak concentration timings, simulations overestimated O₃ and
297 underestimated PM₁₀ at sites with high dust loads, such as Ordos and Kalgan. This

298 discrepancy highlights the challenge of simulating the complex interactions between dust
299 aerosols, precursor gases, and photochemical reactions, particularly in regions with high
300 dust deposition and frequent air pollution episodes. Additionally, the models tended to
301 extend the period of elevated PM₁₀ concentrations beyond the observed time frame,
302 suggesting that the processes controlling dust aerosol removal or dispersion were not fully
303 captured. CHIMERE simulations using J2014 mineralogical data generally outperformed
304 those using J2012 data, with significant reductions in PM₁₀ negative NMBs for three of the
305 four cities, indicating the importance of accurate mineralogical characterization of dust for
306 improving model predictions. When considering the ARI effects of bulk dust aerosols, the
307 underestimation of PM₁₀ was alleviated, whereas the overestimation of O₃ was amplified,
308 which suggests that incorporating ARI effects helps to better represent the impact of dust
309 on local radiative forcing and air quality. Moreover, incorporating ARI effects from the
310 default dust mineralogical atlas further enhanced these trends, underscoring the need for
311 refined aerosol property data in enhancing model performance. Finally, using Earth-
312 observing systems such as the EMIT satellite data led to substantial reductions in PM₁₀
313 negative bias at Kalgan, Beijing, and Tianjin, demonstrating the value of remote sensing
314 data in improving model accuracy, particularly for regions with high aerosol concentrations
315 and complex emission sources. Although considerable progress has been made in dust
316 modeling, notable uncertainties remain. The parameterization of threshold friction velocity
317 and soil texture in emission schemes can still result in underestimated emissions under
318 strong winds (Zuo et al., 2024). Similarly, simplifications in coarse particle size
319 distributions may lead to enhanced deposition and transport losses. In addition, incomplete
320 knowledge of local soil mineralogical composition continues to limit the accurate
321 simulation of both emission fluxes and heterogeneous chemistry (Pang et al., 2024).
322
323



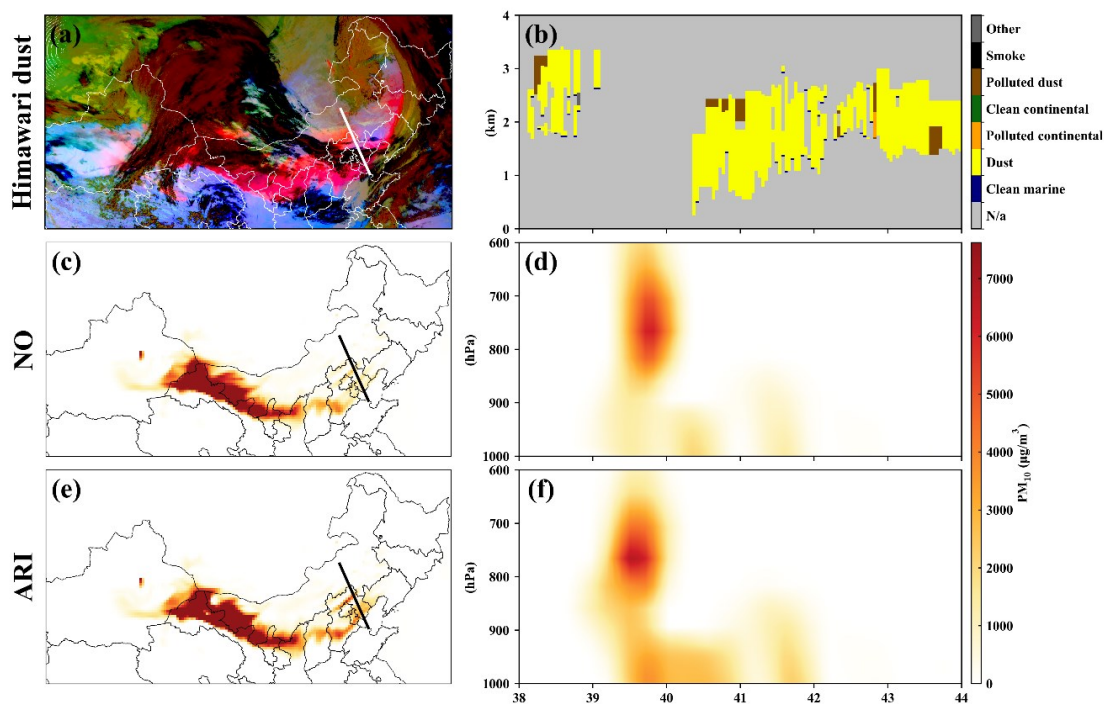
324

325 Figure 2. Statistical metrics between observed and simulated PM_{10} concentrations by different scenario
 326 simulations.

327

328 To evaluate the model performance in simulating the horizontal distribution and
 329 vertical profile of dust aerosol, Figure 3 presents the false RGB imagery of dust derived
 330 from Himawari-8 thermal infrared imagery, along with CALIPSO cross sections of 532 nm
 331 total attenuated backscatter and the vertical feature mask for the overpass of China. The
 332 figure also includes the corresponding spatial distributions of PM_{10} concentrations at 05:00
 333 UTC on 15th March 2021, a time of significant dust transport in the region. This detailed
 334 comparison allows for a comprehensive assessment of how well the model captures both
 335 the horizontal and vertical characteristics of dust aerosol distribution. All six experiments
 336 display similar dust distributions in the atmosphere, consistent with observations from

337 Himawari-8 and CALIPSO. This suggests that the models effectively capture the general
 338 spatial patterns of dust transport. On March 15, 2021, the daily domain-averaged PM₁₀
 339 concentration was 533.81 $\mu\text{g m}^{-3}$, with a 95% confidence interval (CI) of 0.28–5962.95
 340 (Table S2). Specifically, the false RGB imagery from Himawari-8 clearly indicates the
 341 presence of dust plumes in the atmosphere, with distinct thermal contrasts that help identify
 342 the dust layers. The CALIPSO data, which provide vertical profiles of aerosol backscatter,
 343 further validate the model’s ability to capture the vertical extent and concentration of dust
 344 layers. These observations are critical for understanding the atmospheric processes
 345 governing dust dispersion and their impact on air quality. The close agreement between
 346 model simulations and satellite data across all six experiments also underscores the
 347 robustness of the model in representing dust aerosol distribution under different simulation
 348 conditions. This evaluation demonstrates that the models are capable of simulating the
 349 main features of dust aerosol transport, though further refinement in capturing the fine-
 350 scale variations and aerosol properties may still be necessary for more accurate predictions
 351 in future studies.



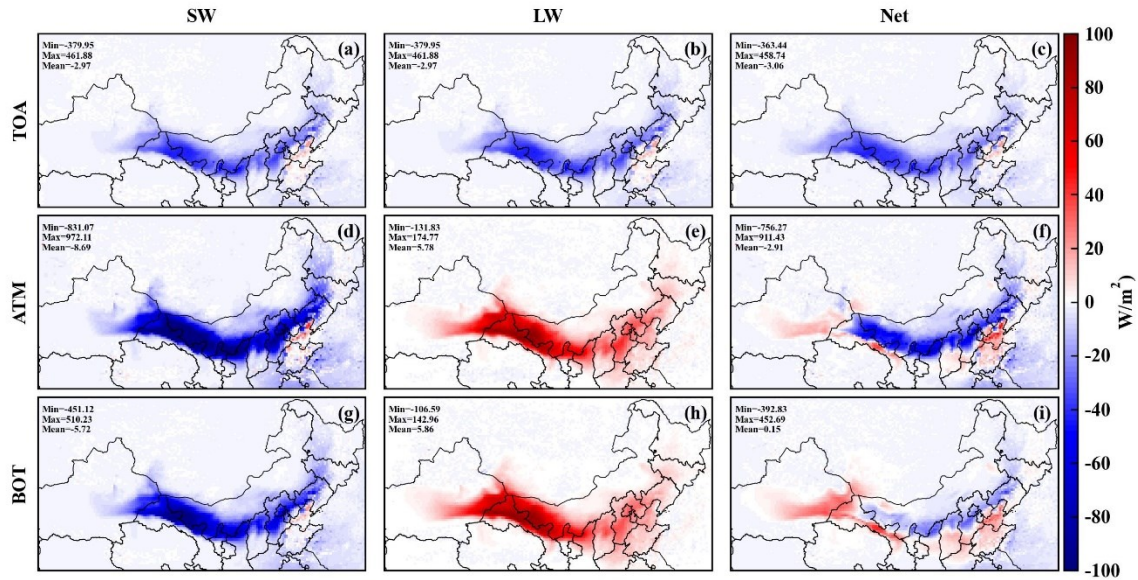
352
 353 Figure 3. The false color imagery of dust from Himawari-8 thermal infrared imagery (a), CALIPSO

354 cross sections of 532 nm total attenuated backscatter and the vertical feature mask for the overpass of
355 China on 13:00 (local time) 15th March 2021 (b), and corresponding horizontal (c and e) and vertical (d
356 and f) distributions of PM₁₀ concentrations.

357 **3.2 Radiative effect on meteorology**

358 To further investigate the impacts of dust radiation on energy balance, the spatial
359 distributions of the average shortwave (SW), longwave (LW), and net (NET) radiative
360 forcing induced by bulk dust on the surface (SFC), in the atmosphere (ATM), and at the
361 top of the atmosphere (TOA) are presented during the dust episode shown in Figure 4. The
362 radiative forcing values provide critical insights into the energy exchanges between dust
363 aerosols and the atmosphere, and their subsequent effects on regional climate dynamics.
364 For SW radiation forcings, dust aerosols produced cooling effects at all three layers: the
365 surface, the atmosphere, and the top of the atmosphere. The average SW radiative forcing
366 was about -5.72 W m^{-2} at the surface, -8.69 W m^{-2} in the atmosphere, and -2.97 W m^{-2}
367 at the TOA, highlighting the significant reduction in solar radiation reaching these layers
368 due to the scattering and absorption properties of the dust particles. Particularly in the dust
369 source regions, the cooling effect at the surface exceeded -900 W m^{-2} (Figures 4a, 4d, and
370 4g), indicating the strong influence of dust on the regional energy budget in these areas.
371 This is a result of the large dust concentrations and their optical properties, which
372 effectively block solar radiation from reaching the Earth's surface. In contrast, the dust-
373 induced LW radiative forcing warmed the surface and atmosphere, with average values
374 ranging from 5.78 to 5.86 W m^{-2} . This warming effect is associated with the absorption of
375 longwave radiation by dust particles, which then re-radiate heat, contributing to local
376 warming. However, dust particles induced negative LW radiative forcing at the TOA, with
377 values ranging from -461.88 to -379.95 W m^{-2} , reflecting the downward flux of longwave
378 radiation absorbed by the aerosols, which reduces the amount of energy reaching the TOA.
379 The NET radiative forcing, which represents the combined effect of both SW and LW
380 forcings, was positive at the surface (about $+0.15 \text{ W m}^{-2}$), negative in the atmosphere
381 (about -2.91 W m^{-2}), and negative at the TOA (about -3.06 W m^{-2}), as shown in Figures
382 4c, 4f, and 4i. The positive NET radiative forcing at the surface suggests a slight net

383 warming effect at ground level, while the negative values in the atmosphere and at the TOA
 384 indicate an overall cooling effect at these higher altitudes.
 385

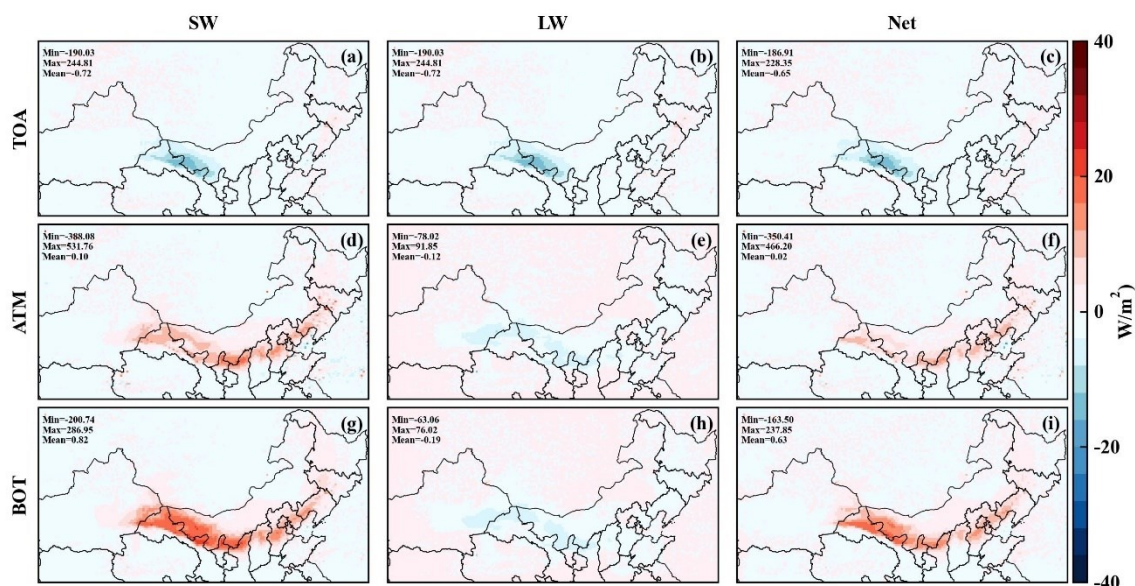


386
 387 Figure 4. Radiation forcings due to bulk dust enabling ARI effects.
 388

389 To assess the impact of dust mineralogical composition on radiative forcings, Figure
 390 S6 illustrates the spatial distribution of radiative differences, considering the ARI effects
 391 of bulk dust and comparing them to the default N2012 mineralogy atlas. This comparison
 392 provides valuable insights into how variations in the mineralogical composition of dust
 393 particles can influence the energy balance in the atmosphere. Compared to the ARI effects
 394 of bulk dust, the mineralogical composition of dust aerosols can lead to increases in SW
 395 radiation forcings at the surface and in the atmosphere, ranging from $+0.10$ to $+0.82 \text{ W m}^{-2}$.
 396 This increase reflects the different optical properties of dust mineral types, which can affect
 397 the scattering and absorption of solar radiation. These variations in the SW radiation
 398 forcings are particularly important for understanding how different dust types modulate the
 399 amount of solar radiation reaching the Earth's surface and atmosphere. At the TOA,
 400 however, the mineralogical composition resulted in a decrease of about -0.72 W m^{-2} in
 401 SW radiation forcing, suggesting that certain mineralogical types may be more efficient at

402 reflecting solar radiation back into space. Similar to SW radiation forcings, net radiation
 403 forcings at the surface and in the atmosphere increased, ranging from +0.02 to +0.63 W
 404 m^{-2} , while at the TOA, net radiation forcings decreased by about -0.65 W m^{-2} . The increase
 405 in net radiation at the surface and in the atmosphere reflects the combined effect of
 406 increased SW absorption and the potential changes in longwave (LW) radiative properties.
 407 For LW radiation forcings, the mineralogical composition of dust led to decreases in the
 408 radiative forcing across different layers, ranging from -0.72 to -0.12 W m^{-2} . This decrease
 409 suggests that certain dust mineral types are more efficient at absorbing and emitting
 410 longwave radiation, which can contribute to cooling effects in the atmosphere and at the
 411 surface.

412



413

414 Figure 5. Difference between TOA, ATM and BOT radiation forcings with considering bulk dust and
 415 mineralogical dust compositions (i.e., N2012_Default) enabling ARI effects.

416

417 As demonstrated in Figure S3, the selection of the soil mineralogy dataset and the
 418 modeling approach significantly influences the calculated dust radiative forcings. When
 419 comparing shortwave dust radiative effects (DRE) from WRF-CHIMERE simulations
 420 using the default N2012 and J2014 mineral atlases, we observe a minor discrepancy in the
 421 DRE amplitude, particularly for shortwave and net radiation forcing at the surface. This

422 discrepancy suggests that the choice of mineralogical dataset can influence the magnitude
423 of radiative forcings, especially under varying atmospheric conditions. Previous research
424 has highlighted the distinct optical properties of hematite and goethite in the shortwave
425 spectrum (Lafon et al., 2006; Sokolik and Toon, 1999). These differences contribute to
426 variations in the dust's radiative properties and, in turn, its effect on energy transfer in the
427 atmosphere. Incorporating both minerals in dust production results in a flatter spectral
428 single scattering albedo (SSA), as goethite's less pronounced dependence on shortwave
429 wavelengths reduces the overall absorption in the shortwave spectrum (Formenti et al.,
430 2014). This effect is particularly noticeable when comparing the radiative forcings from
431 the different mineralogy datasets, as the presence of goethite alters the absorption and
432 scattering characteristics of the dust particles.

433 As depicted in Figure 6, the distinct day-night variations in shortwave radiation
434 forcing (SWRF) induced by ARI effects have been thoroughly demonstrated when
435 considering different mineralogical atlases compared to bulk dust. These variations reflect
436 the different impacts that dust aerosols have on solar radiation during the day and night,
437 with a clear difference in the magnitude of the effects between the two periods. Notably,
438 SWRF variations were more pronounced during the daytime than at night, which can be
439 attributed to the stronger interaction between dust aerosols and incoming solar radiation
440 during daylight hours. The presence of dust aerosols alters the reflection, absorption, and
441 scattering of sunlight, leading to significant changes in the radiation balance, especially
442 during the day when solar energy is at its peak.

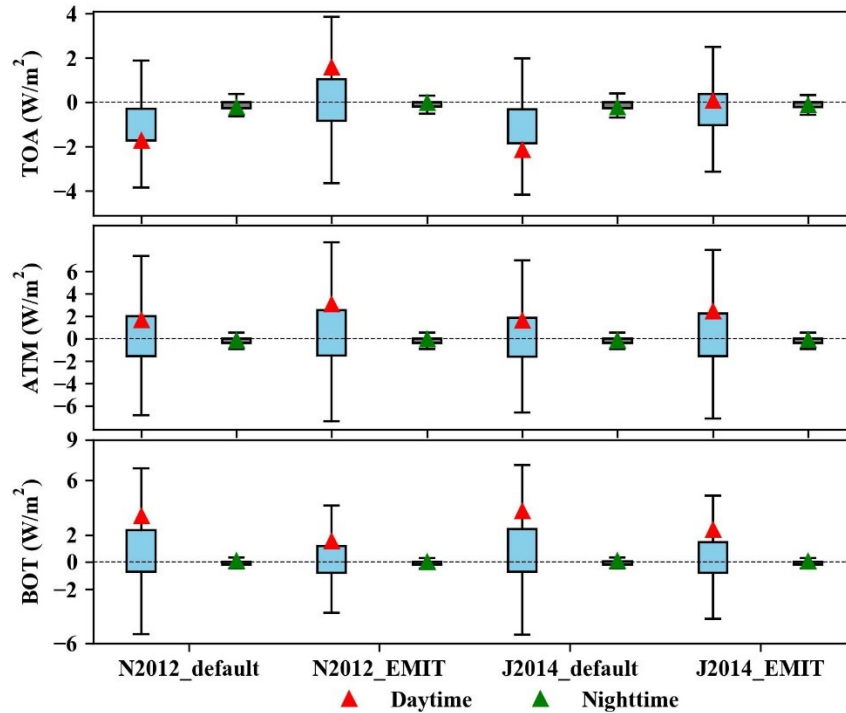
443 Incorporating default dust mineralogical compositions into the simulations led to an
444 increase in daytime SWRF at the surface and within the atmosphere, ranging from 1.60 to
445 3.74 W m^{-2} . This increase suggests that the specific mineralogy of dust aerosols contributes
446 to greater absorption and scattering of solar radiation, amplifying the cooling effect at the
447 surface and the atmosphere. However, at the top of the atmosphere (TOA), the SWRF
448 decreased by approximately 2.00 W m^{-2} , which could be indicative of increased reflection

449 of shortwave radiation back into space due to the dust particles' optical properties. This
450 shift in radiative forcing at the TOA highlights the role of dust in altering the energy fluxes
451 across different atmospheric layers.

452 When comparing simulations using default dust mineralogical compositions to those
453 employing Earth-observing EMIT satellite data within the WRF-CHIMERE model,
454 notable differences in SWRF were observed. Daytime SWRF at the surface was reduced
455 for the N2012 mineralogy dataset (-1.88 W m^{-2}) and J2014 mineralogy dataset (-1.37 W
456 m^{-2}) when using EMIT data, compared to the default dust mineralogy compositions. This
457 reduction could be due to more accurate mineralogical characterization, which alters the
458 dust's optical properties and reduces its ability to absorb and scatter sunlight. Conversely,
459 SWRF was enhanced in the atmosphere (N2012: $+1.44 \text{ W m}^{-2}$, J2014: $+0.84 \text{ W m}^{-2}$) when
460 using the EMIT data, indicating that the updated mineralogical information leads to a
461 different interaction with solar radiation in the atmospheric layer, possibly due to changes
462 in dust composition that affect scattering and absorption properties at higher altitudes.

463 Furthermore, SWRF at the TOA transitioned from negative to positive in simulations
464 using the EMIT data. For the N2012 dataset, the SWRF varied from -1.73 to $+1.59 \text{ W m}^{-2}$,
465 and for the J2014 dataset, it ranged from -2.14 to $+0.07 \text{ W m}^{-2}$. This shift suggests that
466 more accurate dust mineralogy data, particularly from satellite observations, can have a
467 significant impact on the amount of solar radiation reflected back to space, thereby
468 influencing the radiative balance at the TOA. The transition from negative to positive
469 forcing at the TOA emphasizes the importance of incorporating realistic mineralogical
470 information to enhance the accuracy of dust-related radiative forcing calculations and
471 better understand their role in climate systems.

472



473
 474 Figure 6. Day-night changes of TOA, ATM and BOT shortwave radiation forcings from simulations
 475 using different composition atlases (N2012_Default, N2012_EMIT, J2014_Default and J2014_EMIT)
 476 compared to bulk dust.
 477

478 3.3 Radiative effect on air quality

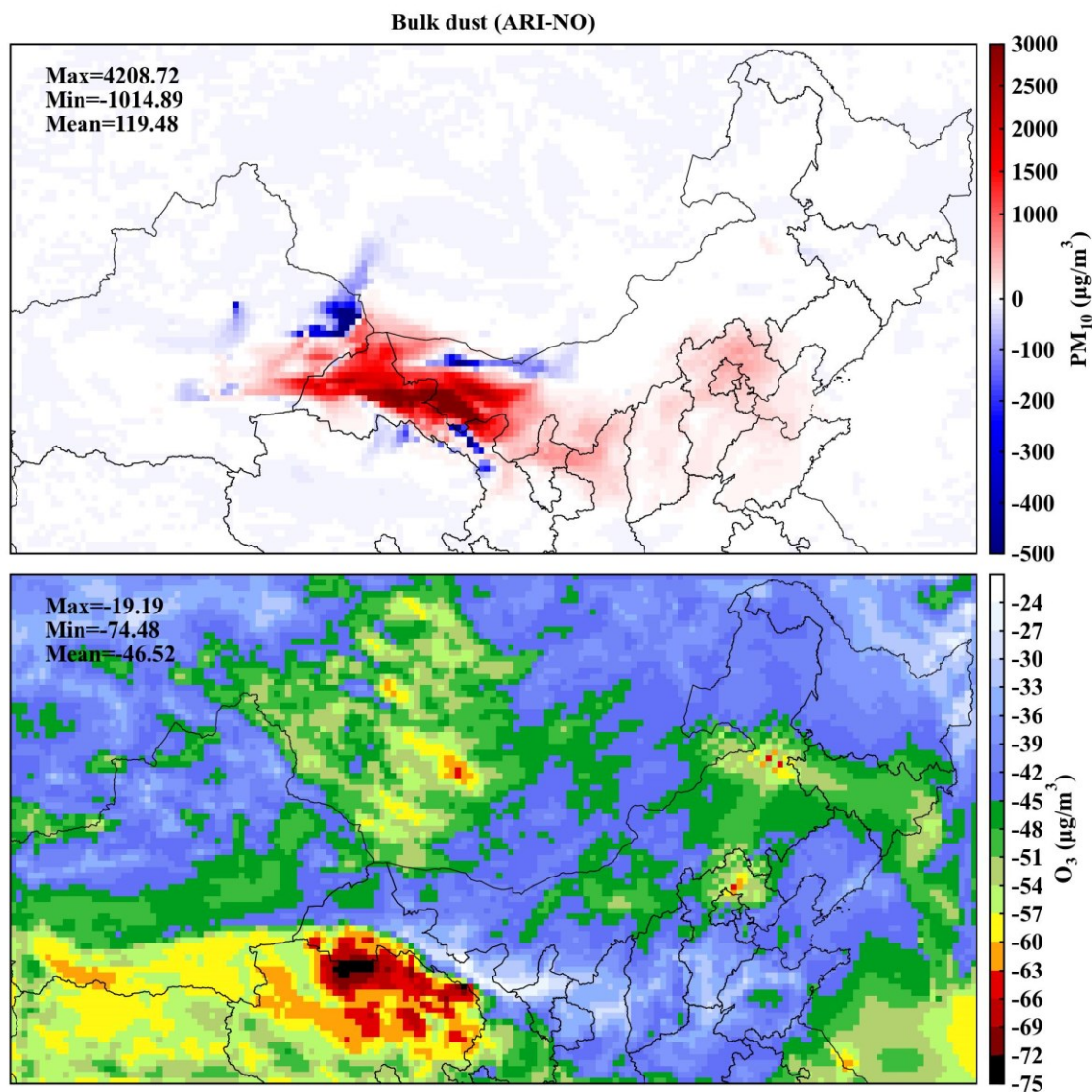
479 Aerosol effects not only gave rise to changes in meteorological variables but also had
 480 a significant impact on air quality. As shown in Figure 7 and Table S3, the inclusion of bulk
 481 dust aerosol feedbacks in the WRF-CHIMERE model resulted in substantial increases in
 482 PM₁₀ concentrations, with an average increase of 119.48 $\mu\text{g m}^{-3}$ with a 95% CI of -27.63
 483 to 1408.39 $\mu\text{g m}^{-3}$. This rise in particulate matter highlights the important role of dust
 484 aerosols in contributing to local and regional air pollution, especially in regions that are
 485 susceptible to dust storms. Along with these increases in PM₁₀ concentrations, O₃
 486 concentrations slightly decreased, with an average reduction of -46.52 $\mu\text{g m}^{-3}$. This
 487 reduction in ozone can be attributed to the complex interaction between dust particles and
 488 ozone precursor gases, where dust aerosols can act as both a sink for ozone and influence
 489 the photochemical processes that govern its formation and degradation. These reactions
 490 would be related to the adsorption and catalytic decomposition of ozone on the surface of

491 mineral dust particles, as well as the potential for dust to alter the concentration of reactive
492 species in the atmosphere through heterogeneous chemistry (Cwiertny et al., 2008). For
493 example, the presence of adsorbed water on dust particles can compete with ozone for
494 reactive sites, reducing the overall uptake and decomposition of ozone (Usher et al., 2003).
495 Additionally, the photochemical reactions involving dust particles, such as the photolysis
496 of nitrate ions, can produce reactive radicals that further influence the atmospheric
497 chemistry of ozone (Ma et al., 2021).

498 The most pronounced increases in PM₁₀ concentrations occurred in the Badain Jaran
499 Desert, a well-known dust source region, where peak values exceeded 1200 $\mu\text{g m}^{-3}$. This
500 reflects the large dust emissions typical of desert environments, where strong winds
501 mobilize vast quantities of particulate matter. Downwind regions, including Ningxia,
502 Shaanxi, and Beijing, also experienced significant PM₁₀ elevations, with concentration
503 differences reaching approximately 600 $\mu\text{g m}^{-3}$ compared to baseline levels. The inclusion
504 of speciated dust influences long-range transport and can substantially affect PM₁₀
505 concentrations. Comparison of the subfigures in Fig. 8 reveals pronounced regional
506 differences in PM₁₀ predictions arising from the use of different mineralogical databases.
507 Incorporating detailed mineralogical data enhances the accuracy of dust composition
508 representation and its associated effects on PM₁₀, highlighting the critical role of mineral
509 speciation in dust modeling and regional air quality assessment.

510 Ozone changes along transport pathways were generally smaller than the surrounding
511 concentrations, typically ranging from -60 to -40 $\mu\text{g m}^{-3}$ with a mean value of -46.52 μg
512 m^{-3} (95% CI: -63.38 to -31.74) as shown in Table S3. These smaller changes in O₃
513 concentrations reflect the fact that dust aerosols have a more localized and complex effect
514 on ozone formation and destruction, with significant variability depending on the regional
515 and temporal context. In particular, dust-induced reductions in ozone are likely to be
516 influenced by the local presence of other atmospheric constituents. The photochemical
517 reactions involving dust particles, such as the photolysis of nitrate ions, can produce

518 reactive radicals that further influence the atmospheric chemistry of ozone (Ma et al., 2021).
519
520



521
522 Figure 7. Changes in PM₁₀ and O₃ concentrations resulting from bulk dust-induced ARI effects,
523 compared to the scenario without aerosol feedbacks.

524

525 The spatial differences in PM₁₀ and O₃ concentrations simulated by WRF-CHIMERE
526 with different mineralogy atlases compared to bulk dust, enabling ARI effects, are depicted
527 in Figures 8 and S4. These comparisons reveal substantial changes in the PM₁₀ and O₃
528 concentrations across the different mineralogical compositions, including N2012_Default,

529 N2012_EMIT, J2014_Default, J2014_EMIT, and bulk dust. This suggests that the
530 normalization of the 12 minerals from these atlases significantly modifies meteorological
531 conditions, further influencing the relative abundances of dust particles and their
532 subsequent effects on air quality and atmospheric composition.

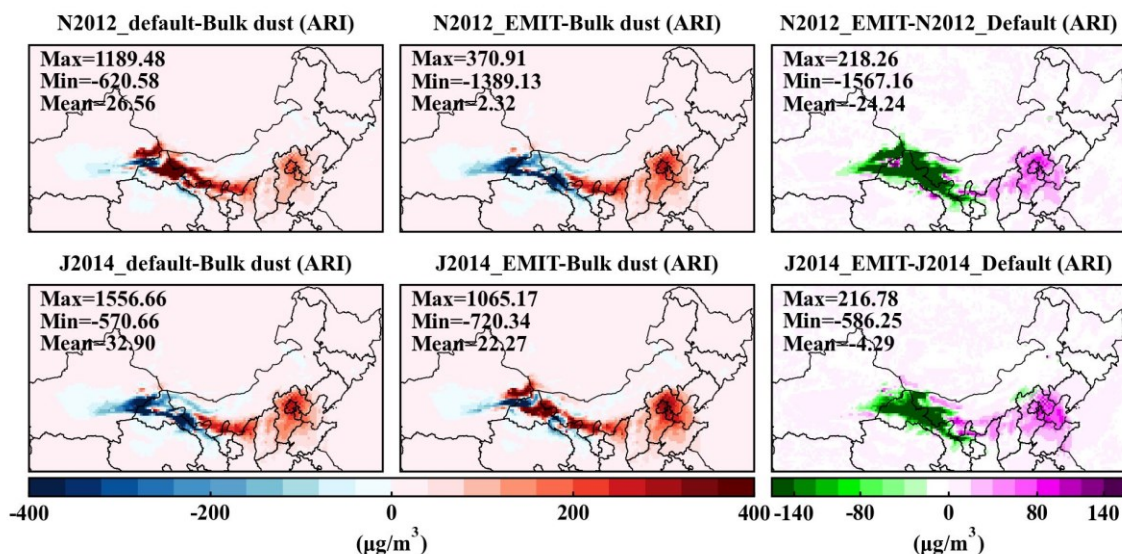
533 When compared to bulk dust, reduced PM₁₀ concentrations were primarily observed
534 in the Taklimakan Desert, with decreases of around 60 μg m⁻³, while increases in PM₁₀
535 concentrations occurred in the Badain Jaran Desert and its downwind regions, with
536 concentrations rising up to 1000 μg m⁻³. These regional variations indicate that different
537 dust mineralogical compositions can impact the emission and transport of dust, with certain
538 mineral types leading to more efficient scattering or absorption of radiation, which may
539 alter the local meteorological conditions and dust dispersion patterns.

540 For O₃ concentrations, reductions and enhancements were mainly observed in the
541 Horqin sandy land and North China Plain, with changes up to 4 μg m⁻³, respectively. This
542 highlights the complex interaction between dust aerosols and ozone chemistry, where dust
543 can either enhance or reduce ozone concentrations depending on the region. Dust aerosols
544 can influence ozone levels by acting as a surface for heterogeneous chemical reactions or
545 by modifying the photochemical processes that control ozone formation and destruction.

546 When considering the EMIT data, PM₁₀ concentrations were reduced in dust source
547 regions and enhanced in downwind regions, with reductions of up to -1567.16 μg m⁻³ and
548 increases of +218.26 μg m⁻³. This suggests that more accurate mineralogical data can
549 influence dust transport patterns, leading to greater reductions in PM₁₀ at the source regions
550 and increased dust concentrations in the downwind areas. These findings further emphasize
551 the role of mineralogical composition in modulating dust aerosol behavior and distribution.

552 For O₃, enhancements appeared in source regions, while reductions were observed in
553 downwind regions, with changes ranging from -2.46 to +3.52 μg m⁻³. These trends suggest
554 that more accurate dust speciation can influence regional ozone levels in different ways,
555 with possible implications for local air quality and atmospheric chemistry. Notably, the

556 impacts on PM₁₀ concentrations from N2012_EMIT compared to N2012_Default were
 557 larger than those observed from J2014_EMIT versus J2014_Default, while the impacts on
 558 O₃ concentrations followed the opposite trends. This indicates that the choice of dust
 559 mineralogical dataset has a differential impact on PM₁₀ and O₃ concentrations,
 560 underscoring the importance of considering mineral composition in aerosol modeling to
 561 more accurately predict air quality and climate effects.
 562



563
 564 Figure 8. Difference in PM₁₀ concentrations considering bulk dust and various dust mineralogy atlases
 565 that enable ARI effects.
 566

567 Figure 9 shows the percentage changes in surface concentrations of mineral dust with
 568 and without considering ARI effects. These results provide valuable insight into how the
 569 inclusion of ARI effects modifies the composition and radiative properties of dust aerosols,
 570 depending on the mineralogical dataset used. For the N2012_Default and N2012_EMIT
 571 data, quartz and feldspar accounted for a substantial portion of the total dust, ranging from
 572 approximately 51.7% to 57.4% for quartz and 18.6% to 19.8% for feldspar. This indicates
 573 that quartz and feldspar are the dominant mineral components in the dust modeled with the
 574 N2012 dataset.

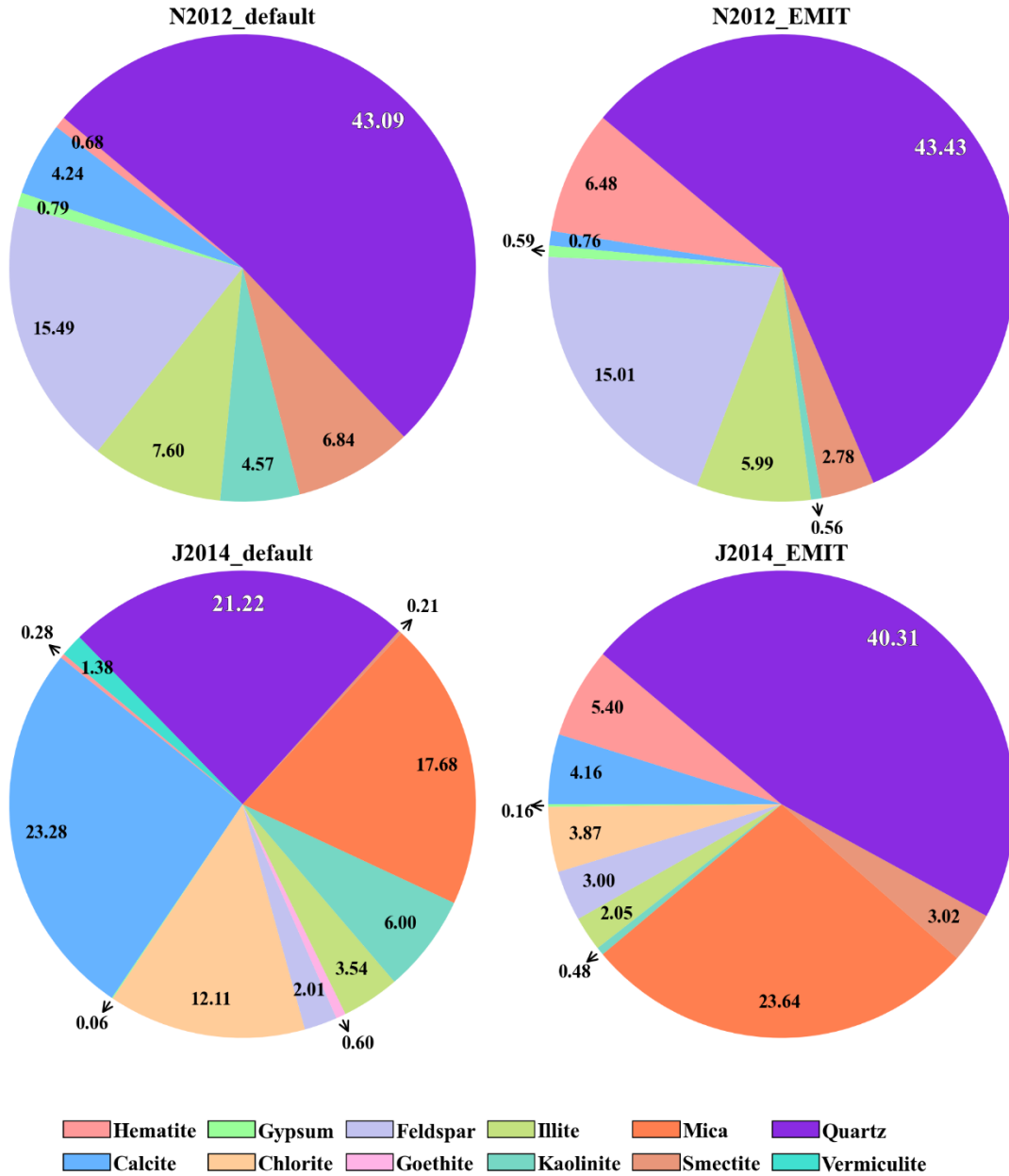
575 In contrast, for the J2014_Default dataset, the mineral composition was more

576 diversified, with calcite, quartz, and mica contributing about 26.3%, 24.0%, and 20.0%,
577 respectively, to the total dust composition. This shift in mineral proportions reflects the
578 differences in the mineralogical characterization between the N2012 and J2014 datasets,
579 with J2014 incorporating a broader range of dust minerals. For J2014_EMIT, the mineral
580 composition shifted further, with quartz and mica making up approximately 46.8% and
581 27.5% of the dust, respectively. This highlights the importance of using accurate
582 mineralogical data, such as that from EMIT satellite observations, to better represent the
583 composition of dust aerosols in simulations.

584 The inclusion of EMIT data led to an increase in the absorption percentage of hematite
585 by about 8% for N2012 and 6% for J2014. Hematite is a highly absorbing mineral,
586 especially in the shortwave spectrum, and its increased presence enhances the dust's ability
587 to absorb solar radiation, thereby affecting the DRE in the shortwave spectrum. This
588 increase in hematite absorption is significant, as it directly impacts the radiative effects of
589 dust, potentially contributing to a greater cooling effect on the atmosphere by modifying
590 the shortwave radiation balance.

591 While quartz constitutes the largest portion of the dust in both the N2012 and J2014
592 datasets, its DRF effects are relatively limited, as noted in Li et al. (2021). Quartz is known
593 for its high reflectivity in the shortwave spectrum, and while it makes up a large fraction
594 of the total dust mass, it has a less pronounced effect on radiative forcing compared to more
595 absorbing minerals like hematite or mica. This suggests that, despite its dominance in dust
596 composition, quartz plays a smaller role in modifying the energy balance of the atmosphere
597 through direct radiative effects.

598
599



600
 601 Figure 9. Contributions of different mineralogical compositions using N2012_Default, N2012_EMIT,
 602 J2014_Default, and J2014_EMIT, considering ARI effects, compared to the scenario without enabling
 603 aerosol feedbacks.
 604

605 3.4 Limitations and uncertainties for aerosol feedbacks of mineralogical dust

606 The accuracy of simulated dust emission is intricately linked to soil properties, such
 607 as soil texture and moisture, which primarily influence the threshold friction velocity
 608 required for dust particle mobilization (Kim and Choi, 2015; Su and Fung, 2015). These

609 factors play a critical role in determining the magnitude and spatial distribution of dust
610 emissions, underscoring the need for precise and high-resolution soil data in dust modeling.
611 While the current EMIT L3 data offers a spatial resolution of $0.5^\circ \times 0.5^\circ$, real-time higher
612 spatial resolution datasets, such as the $60 \text{ m} \times 60 \text{ m}$ EMIT L2B mineral atlas
613 (https://earth.jpl.nasa.gov/emit/internal_resources/282), can provide a more detailed
614 representation of soil mineralogy, thereby enhancing the fidelity of dust emission
615 simulations.

616 The uncertainty associated with dust mineralogical datasets is being actively
617 addressed by NASA's EMIT. This initiative has deployed a hyperspectral imaging
618 spectrometer aboard the International Space Station to deliver global retrievals of soil
619 mineral compositions with unprecedented spatial detail. The spectrometer captures spectral
620 absorption features within the UV to near-infrared range ($0.38\text{--}2.5 \mu\text{m}$), offering critical
621 insights into the distribution and variability of soil minerals (Castellanos et al., 2024;
622 Connelly et al., 2021). In addition to satellite-based observations, ground-based stations
623 play a vital role in measuring dust mineralogical compositions using stationary instruments,
624 which provide localized and highly accurate data. Complementing these measurements,
625 aircraft-based instruments offer the capability to sample dust particles along specific flight
626 tracks, providing valuable vertical and spatial profiles of speciated dust properties (e.g.,
627 size and mixing state, Panta et al., 2023; Ryder et al., 2015). Together, these observational
628 platforms form a robust foundation for validating and improving dust models.

629 Aerosol-cloud interactions involving speciated dust are another critical aspect of dust-
630 climate interactions that require further investigation, especially for feldspar and quartz
631 (Atkinson et al., 2013; Chatziparaschos et al., 2023). Incorporating these interactions into
632 two-way coupled WRF-CHIMERE models can provide a more comprehensive
633 understanding of the feedback mechanisms between dust aerosols and cloud microphysics.
634 Such implementations are currently a focus of ongoing work, aiming to refine the
635 representation of dust-induced radiative and microphysical effects in regional and global

636 models. These efforts will not only improve model accuracy but also enhance our ability
637 to predict the impacts of dust on weather, air quality, and climate.

638

639 **4 Conclusion**

640 Dust mineral composition plays a vital role in regulating atmospheric radiation and
641 air quality, yet its effects remain poorly constrained in current atmospheric models.
642 Understanding these impacts is particularly important for North China, where severe dust
643 storms frequently affect regional climate and pollution. This study investigates how
644 variations in mineral composition influence aerosol–radiation interactions and their
645 implications for meteorology and air quality during a major dust storm event.

646 The findings revealed significant spatial variations in radiative forcing due to
647 differences in dust mineralogy. Compared to the ARI effects of bulk dust, the mineralogical
648 composition of dust aerosols can increase SW radiation forcing at the surface and in the
649 atmosphere by +0.10 to +0.82 W m⁻², while simultaneously causing a decrease of
650 approximately -0.72 W m⁻² in SW radiation forcing at the TOA. Integrating EMIT data
651 into the model reduced PM₁₀ biases by over 15% in high-concentration regions and
652 improved ozone predictions, with localized changes ranging from -2.46 to +3.52 μg m⁻³.
653 Specifically, the ARI effects of these mineralogical compositions led to a notable increase
654 in PM₁₀ levels, reaching up to 1189.48 μg m⁻³ in dust source regions, when compared to
655 bulk dust scenarios.

656 These findings highlight the importance of incorporating dust mineralogical data to
657 improve simulations of radiative forcing and air quality impacts. Within the scope of this
658 study, the results indicate that overall dust mineralogical composition, rather than dust mass
659 alone, plays a decisive role in ARI effects, with hematite exerting a dominant influence
660 despite its minor abundance, although the radiative effects of individual mineral species
661 were not separately quantified. Systematic biases in surface radiation, near-surface winds,
662 and temperature persist, reflecting challenges in simulating dust–atmosphere interactions
663 and uncertainties in mineralogical datasets. Incorporating meteorological spectral nudging

664 in future simulations could provide a more realistic representation of ARI-induced dust
665 perturbations under different mineralogical compositions. Coupling this approach with
666 higher-resolution soil and satellite data, as well as additional observational constraints,
667 would further refine dust emission simulations and reduce model biases, particularly in
668 regions frequently affected by severe dust events.

669

670 **Data and software availability**

671 The meteorological ICs and BCs, Chemical ICs and BCs and emission data used for
672 WRF–CHIMERE and all data used to create figures and tables in this study are provided
673 in an open repository on Zenodo (<https://doi.org/10.5281/zenodo.14728874>, Gao et al.,
674 2025a). Himawari and CALIPSO satellite data are available at
675 <ftp://ftp.ptree.jaxa.jp/jma/netcdf> and <https://subset.larc.nasa.gov/calipso>, respectively.

676 The source codes of the two-way coupled WRFv3.7.1–CHIMERE v2020r3 models
677 are obtained from <https://www.lmd.polytechnique.fr/chimere>. The related source codes,
678 configuration information, namelist files and automated run scripts of these three two-way
679 coupled models are archived at Zenodo with the following associated DOI:
680 <https://doi.org/10.5281/zenodo.14729124> (Gao et al., 2025b).

681

682 **Author contributions**

683 CG, XZ, HY and LH carried out the data collection, related analysis, figure plotting,
684 and paper writing. HZ, SZ, and AX were involved with the original research plan and made
685 suggestions for the paper writing.

686 **Competing interests**

687 The contact author has declared that neither they nor their co-authors have any
688 competing interests.

689

690 **Acknowledgments**

691 This study was financially sponsored by the National Natural Science Foundation of
692 China (grant nos. 42305171, 42371154 & 42171142), the Natural Science Foundation of

693 Jilin Province (YDZJ202201ZYTS476), the National Key Scientific and Technological
694 Infrastructure project “Earth System Numerical Simulation Facility” (2023-EL-PT-
695 000469), the Youth Innovation Promotion Association of Chinese Academy of Sciences,
696 China (grant nos. 2022230), the National Key Research and Development Program of
697 China (grant nos. 2017YFC0212304 & 2019YFE0194500) and the Talent Program of
698 Chinese Academy of Sciences (Y8H1021001).

699

700 Reference

- 701 Adebisi, A., Kok, J. F., Murray, B. J., Ryder, C. L., Stuut, J.-B. W., Kahn, R. A., Knippertz, P., Formenti,
702 P., Mahowald, N. M., and García-Pando, C. P.: A review of coarse mineral dust in the Earth
703 system, *Aeolian Research*, 60, 100849, <https://doi.org/10.1016/j.aeolia.2022.100849>, 2023.
- 704 Alfaro, S., Lafon, S., Rajot, J., Formenti, P., Gaudichet, A., and Maille, M.: Iron oxides and light
705 absorption by pure desert dust: An experimental study, *Journal of Geophysical Research:*
706 *Atmospheres*, 109, <https://doi.org/10.1029/2003JD004374>, 2004.
- 707 Atkinson, J. D., Murray, B. J., Woodhouse, M. T., Whale, T. F., Baustian, K. J., Carslaw, K. S., Dobbie,
708 S., O’Sullivan, D., and Malkin, T. L.: The importance of feldspar for ice nucleation by mineral
709 dust in mixed-phase clouds, *Nature*, 498, 355–358, <https://doi.org/10.1038/nature12278>, 2013.
- 710 Balkanski, Y., Bonnet, R., Boucher, O., Checa-Garcia, R., and Servonnat, J.: Better representation of
711 dust can improve climate models with too weak an African monsoon, *Atmospheric Chemistry*
712 *and Physics*, 21, 11423–11435, <https://doi.org/10.5194/acp-21-11423-2021>, 2021.
- 713 Briant, R., Tuccella, P., Deroubaix, A., Khvorostyanov, D., Menut, L., Mailler, S., and Turquety, S.:
714 Aerosol–radiation interaction modelling using online coupling between the WRF 3.7.1
715 meteorological model and the CHIMERE 2016 chemistry-transport model, through the
716 OASIS3-MCT coupler, *Geosci. Model Dev.*, 10, 927–944, <https://doi.org/10.5194/gmd-10-927-2017>, 2017.
- 718 Castellanos, P., Colarco, P., Espinosa, W. R., Guzewich, S. D., Levy, R. C., Miller, R. L., Chin, M., Kahn,
719 R. A., Kemppinen, O., and Moosmüller, H.: Mineral dust optical properties for remote sensing
720 and global modeling: A review, *Remote Sensing of Environment*, 303, 113982,
721 <https://doi.org/10.1016/j.rse.2023.113982>, 2024.
- 722 Chatziparaschos, M., Daskalakis, N., Myriokefalitakis, S., Kalivitis, N., Nenes, A., Gonçalves Ageitos,
723 M., Costa-Surós, M., Pérez García-Pando, C., Zanolli, M., Vrekoussis, M., and Kanakidou, M.:
724 Role of K-feldspar and quartz in global ice nucleation by mineral dust in mixed-phase clouds,
725 *Atmos. Chem. Phys.*, 23, 1785–1801, <https://doi.org/10.5194/acp-23-1785-2023>, 2023.
- 726 Choobari, O. A., Zawar-Reza, P., and Sturman, A.: The global distribution of mineral dust and its
727 impacts on the climate system: A review, *Atmospheric Research*, 138, 152–165,
728 <https://doi.org/10.1016/j.atmosres.2013.11.007>, 2014.
- 729 Claquin, T., Schulz, M., and Balkanski, Y.: Modeling the mineralogy of atmospheric dust sources,
730 *Journal of Geophysical Research: Atmospheres*, 104, 22243–22256,

731 <https://doi.org/10.1029/1999JD900416>, 1999.

732 Connelly, D. S., Thompson, D. R., Mahowald, N. M., Li, L., Carmon, N., Okin, G. S., and Green, R. O.:

733 The EMIT mission information yield for mineral dust radiative forcing, *Remote Sensing of*

734 *Environment*, 258, 112380, <https://doi.org/10.1016/j.rse.2021.112380>, 2021.

735 Cwiertny, D. M., Young, M. A., and Grassian, V. H.: Chemistry and photochemistry of mineral dust

736 aerosol, *Annu. Rev. Phys. Chem.*, 59, 27–51,

737 <https://doi.org/10.1146/annurev.physchem.59.032607.093630>, 2008.

738 Duniway, M. C., Pfennigwerth, A. A., Fick, S. E., Nauman, T. W., Belnap, J., and Barger, N. N.: Wind

739 erosion and dust from US drylands: a review of causes, consequences, and solutions in a

740 changing world, *Ecosphere*, 10, e02650, <https://doi.org/10.1002/ecs2.2650>, 2019.

741 Fécan, F., Marticorena, B., and Bergametti, G.: Parametrization of the increase of the aeolian erosion

742 threshold wind friction velocity due to soil moisture for arid and semi-arid areas, *Annales*

743 *Geophysicae*, 17, 149–157, <https://doi.org/10.1007/s00585-999-0149-7>, 1998.

744 Formenti, P., Caquineau, S., Desboeufs, K., Klaver, A., Chevaillier, S., Journet, E., and Rajot, J.-L.:

745 Mapping the physico-chemical properties of mineral dust in western Africa: mineralogical

746 composition, *Atmospheric Chemistry and Physics*, 14, 10663–10686,

747 <https://doi.org/10.5194/acp-14-10663-2014>, 2014.

748 Gao, C., Xiu, A., Zhang, X., Tong, Q., Zhao, H., Zhang, S., Yang, G., and Zhang, M.: Two-way coupled

749 meteorology and air quality models in Asia: a systematic review and meta-analysis of impacts

750 of aerosol feedbacks on meteorology and air quality, *Atmos. Chem. Phys.*, 22, 5265–5329,

751 <https://doi.org/10.5194/acp-22-5265-2022>, 2022.

752 Gómez Maqueo Anaya, S., Althausen, D., Faust, M., Baars, H., Heinold, B., Hofer, J., Tegen, I.,

753 Ansmann, A., Engelmann, R., and Skupin, A.: The implementation of dust mineralogy in

754 COSMO5. 05-MUSCAT, *Geoscientific Model Development*, 17, 1271–1295,

755 <https://doi.org/10.5194/gmd-17-1271-2024>, 2024.

756 Gonçalves Ageitos, M., Obiso, V., Miller, R. L., Jorba, O., Klose, M., Dawson, M., Balkanski, Y.,

757 Perlwitz, J., Basart, S., Di Tomaso, E., Escribano, J., Macchia, F., Montané, G., Mahowald, N.

758 M., Green, R. O., Thompson, D. R., and Pérez García-Pando, C.: Modeling dust mineralogical

759 composition: sensitivity to soil mineralogy atlases and their expected climate impacts, *Atmos.*

760 *Chem. Phys.*, 23, 8623–8657, <https://doi.org/10.5194/acp-23-8623-2023>, 2023.

761 Green, R. O., Mahowald, N., Ung, C., Thompson, D. R., Bator, L., Bennet, M., Bernas, M., Blackway,

762 N., Bradley, C., and Cha, J.: The Earth surface mineral dust source investigation: An Earth

763 science imaging spectroscopy mission, 2020 IEEE aerospace conference, 1–15, 2020.

764 Harrison, A. D., Whale, T. F., Carpenter, M. A., Holden, M. A., Neve, L., O’Sullivan, D., Vergara

765 Temprado, J., and Murray, B. J.: Not all feldspars are equal: a survey of ice nucleating

766 properties across the feldspar group of minerals, *Atmos. Chem. Phys.*, 16, 10927–10940,

767 <https://doi.org/10.5194/acp-16-10927-2016>, 2016.

768 Journet, E., Balkanski, Y., and Harrison, S. P.: A new data set of soil mineralogy for dust-cycle modeling,

769 *Atmos. Chem. Phys.*, 14, 3801–3816, <https://doi.org/10.5194/acp-14-3801-2014>, 2014.

770 Ke, Z., Liu, X., Wu, M., Shan, Y., and Shi, Y.: Improved dust representation and impacts on dust

771 transport and radiative effect in CAM5, *Journal of Advances in Modeling Earth Systems*, 14,

772 e2021MS002845, <https://doi.org/10.1029/2021MS002845>, 2022.

773 Kim, H. and Choi, M.: Impact of soil moisture on dust outbreaks in East Asia: Using satellite and
774 assimilation data, *Geophysical Research Letters*, 42, 2789–2796,
775 <https://doi.org/10.1002/2015GL063325>, 2015.

776 Klingmüller, K., Lelieveld, J., Karydis, V. A., and Stenchikov, G. L.: Direct radiative effect of dust–
777 pollution interactions, *Atmospheric Chemistry and Physics*, 19, 7397–7408,
778 <https://doi.org/10.5194/acp-19-7397-2019>, 2019.

779 Kok, J., Mahowald, N., Fratini, G., Gillies, J., Ishizuka, M., Leys, J., Mikami, M., Park, M.-S., Park, S.-
780 U., and Van Pelt, R.: An improved dust emission model–Part 1: Model description and
781 comparison against measurements, *Atmospheric Chemistry and Physics*, 14, 13023–13041,
782 <https://doi.org/10.5194/acp-14-13023-2014>, 2014.

783 Kok, J. F., Ridley, D. A., Zhou, Q., Miller, R. L., Zhao, C., Heald, C. L., Ward, D. S., Albani, S., and
784 Haustein, K.: Smaller desert dust cooling effect estimated from analysis of dust size and
785 abundance, *Nature Geoscience*, 10, 274–278, <https://doi.org/10.1038/ngeo2912>, 2017.

786 Kok, J. F., Storelvmo, T., Karydis, V. A., Adebisi, A. A., Mahowald, N. M., Evan, A. T., He, C., and
787 Leung, D. M.: Mineral dust aerosol impacts on global climate and climate change, *Nature*
788 *Reviews Earth & Environment*, 4, 71–86, <https://doi.org/10.1038/s43017-022-00379-5>, 2023.

789 Kumar, A., Marcolli, C., Luo, B., and Peter, T.: Ice nucleation activity of silicates and aluminosilicates
790 in pure water and aqueous solutions–Part 1: The K-feldspar microcline, *Atmospheric Chemistry*
791 *and Physics*, 18, 7057–7079, <https://doi.org/10.5194/acp-18-7057-2018>, 2018.

792 Lafon, S., Sokolik, I. N., Rajot, J. L., Caqueneau, S., and Gaudichet, A.: Characterization of iron oxides
793 in mineral dust aerosols: Implications for light absorption, *Journal of Geophysical Research:*
794 *Atmospheres*, 111, <https://doi.org/10.1029/2005JD007016>, 2006.

795 Li, L. and Sokolik, I. N.: The dust direct radiative impact and Its sensitivity to the land surface state and
796 key minerals in the WRF-Chem-DuMo Model: a case study of dust storms in Central Asia,
797 *Journal of Geophysical Research: Atmospheres*, 123, 4564–4582,
798 <https://doi.org/10.1029/2017JD027667>, 2018.

799 Li, L., Mahowald, N. M., Miller, R. L., Pérez García-Pando, C., Klose, M., Hamilton, D. S., Gonçalves
800 Ageitos, M., Ginoux, P., Balkanski, Y., Green, R. O., Kalashnikova, O., Kok, J. F., Obiso, V.,
801 Paynter, D., and Thompson, D. R.: Quantifying the range of the dust direct radiative effect due
802 to source mineralogy uncertainty, *Atmos. Chem. Phys.*, 21, 3973–4005,
803 <https://doi.org/10.5194/acp-21-3973-2021>, 2021.

804 Li, L., Mahowald, N. M., Kok, J. F., Liu, X., Wu, M., Leung, D. M., Hamilton, D. S., Emmons, L. K.,
805 Huang, Y., Sexton, N., Meng, J., and Wan, J.: Importance of different parameterization changes
806 for the updated dust cycle modeling in the Community Atmosphere Model (version 6.1), *Geosci.*
807 *Model Dev.*, 15, 8181–8219, <https://doi.org/10.5194/gmd-15-8181-2022>, 2022.

808 Li, L., Mahowald, N. M., Gonçalves Ageitos, M., Obiso, V., Miller, R. L., Pérez García-Pando, C., Di
809 Biagio, C., Formenti, P., Brodrick, P. G., and Clark, R. N.: Improved constraints on hematite
810 refractive index for estimating climatic effects of dust aerosols, *Communications Earth &*
811 *Environment*, 5, 295, <https://doi.org/10.1038/s43247-024-01441-4>, 2024.

812 Ma, Q., Zhong, C., Ma, J., Ye, C., Zhao, Y., Liu, Y., Zhang, P., Chen, T., Liu, C., and Chu, B.:

813 Comprehensive study about the photolysis of nitrates on mineral oxides, *Environmental*
814 *Science & Technology*, 55, 8604–8612, <https://doi.org/10.1021/acs.est.1c02182>, 2021.

815 Maher, B. A., Prospero, J. M., Mackie, D., Gaiero, D., Hesse, P. P., and Balkanski, Y.: Global
816 connections between aeolian dust, climate and ocean biogeochemistry at the present day and at
817 the last glacial maximum, *Earth-Science Reviews*, 99, 61–97,
818 <https://doi.org/10.1016/j.earscirev.2009.12.001>, 2010.

819 Menut, L., Siour, G., Bessagnet, B., Couvidat, F., Journet, E., Balkanski, Y., and Desboeufs, K.:
820 Modelling the mineralogical composition and solubility of mineral dust in the Mediterranean
821 area with CHIMERE 2017r4, *Geosci. Model Dev.*, 13, 2051–2071,
822 <https://doi.org/10.5194/gmd-13-2051-2020>, 2020.

823 Menut, L., Bessagnet, B., Cholakian, A., Siour, G., Mailler, S., and Pennel, R.: What is the relative
824 impact of nudging and online coupling on meteorological variables, pollutant concentrations
825 and aerosol optical properties?, *Geoscientific Model Development*, 17, 3645–3665,
826 <https://doi.org/10.5194/gmd-17-3645-2024>, 2024.

827 Nickovic, S., Vukovic, A., Vujadinovic, M., Djurdjevic, V., and Pejanovic, G.: Technical Note: High-
828 resolution mineralogical database of dust-productive soils for atmospheric dust modeling,
829 *Atmos. Chem. Phys.*, 12, 845–855, <https://doi.org/10.5194/acp-12-845-2012>, 2012.

830 Obiso, V., Gonçalves Ageitos, M., Pérez García-Pando, C., Perlwitz, J. P., Schuster, G. L., Bauer, S. E.,
831 Di Biagio, C., Formenti, P., Tsigaridis, K., and Miller, R. L.: Observationally constrained
832 regional variations of shortwave absorption by iron oxides emphasize the cooling effect of dust,
833 *Atmospheric Chemistry and Physics*, 24, 5337–5367, [https://doi.org/10.5194/acp-24-5337-](https://doi.org/10.5194/acp-24-5337-2024)
834 [2024](https://doi.org/10.5194/acp-24-5337-2024), 2024.

835 Pang, M., Jin, J., Segers, A., Jiang, H., Han, W., Buyantogtokh, B., Xia, J., Fang, L., Li, J., and Lin, H.
836 X.: Valid time shifting ensemble Kalman filter (VTS-EnKF) for dust storm forecasting,
837 *Geoscientific Model Development*, 17, 8223–8242, [https://doi.org/10.5194/gmd-17-8223-](https://doi.org/10.5194/gmd-17-8223-2024)
838 [2024](https://doi.org/10.5194/gmd-17-8223-2024), 2024.

839 Panta, A., Kandler, K., Alastuey, A., González-Flórez, C., González-Romero, A., Klose, M., Querol, X.,
840 Reche, C., Yus-Díez, J., and Pérez García-Pando, C.: Insights into the single-particle
841 composition, size, mixing state, and aspect ratio of freshly emitted mineral dust from field
842 measurements in the Moroccan Sahara using electron microscopy, *Atmospheric Chemistry and*
843 *Physics*, 23, 3861–3885, <https://doi.org/10.5194/acp-23-3861-2023>, 2023.

844 Ryder, C., McQuaid, J. B., Flamant, C., Rosenberg, P., Washington, R., Brindley, H., Highwood, E.,
845 Marsham, J., Parker, D., and Todd, M.: Advances in understanding mineral dust and boundary
846 layer processes over the Sahara from Fennec aircraft observations, *Atmospheric Chemistry and*
847 *Physics*, 15, 8479–8520, <https://doi.org/10.5194/acp-15-8479-2015>, 2015.

848 Scanza, R. A., Mahowald, N., Ghan, S., Zender, C. S., Kok, J. F., Liu, X., Zhang, Y., and Albani, S.:
849 Modeling dust as component minerals in the Community Atmosphere Model: development of
850 framework and impact on radiative forcing, *Atmos. Chem. Phys.*, 15, 537–561,
851 <https://doi.org/10.5194/acp-15-537-2015>, 2015.

852 Schepanski, K.: Transport of mineral dust and its impact on climate, *Geosciences*, 8, 151,
853 <https://doi.org/10.3390/geosciences8050151>, 2018.

854 Shao, Y. and Lu, H.: A simple expression for wind erosion threshold friction velocity, *Journal of*
855 *Geophysical Research: Atmospheres*, 105, 22437–22443,
856 <https://doi.org/10.1029/2000JD900304>, 2000.

857 Shao, Y., Wyrwoll, K.-H., Chappell, A., Huang, J., Lin, Z., McTainsh, G. H., Mikami, M., Tanaka, T. Y.,
858 Wang, X., and Yoon, S.: Dust cycle: An emerging core theme in Earth system science, *Aeolian*
859 *Research*, 2, 181–204, <https://doi.org/10.1016/j.aeolia.2011.02.001>, 2011.

860 Sokolik, I. N. and Toon, O. B.: Incorporation of mineralogical composition into models of the radiative
861 properties of mineral aerosol from UV to IR wavelengths, *J. Geophys. Res.*, 104, 9423–9444,
862 <https://doi.org/10.1029/1998JD200048>, 1999.

863 Solomos, S., Spyrou, C., Bartsotas, N. S., Sykioti, O., Amiridis, V., Gkikas, A., Marinou, E., Katsafados,
864 P., Tsarpalis, K., and Pejanovic, G.: The Development of a Dust Mineralogy Map from Satellite
865 Retrievals and Implementation in WRF-Chem, *Environmental Sciences Proceedings*, 26, 54,
866 <https://doi.org/10.3390/envirosciproc2023026054>, 2023a.

867 Solomos, S., Spyrou, C., Barreto, A., Rodríguez, S., González, Y., Neophytou, M. K., Mouzourides, P.,
868 Bartsotas, N. S., Kalogeri, C., and Nickovic, S.: The development of METAL-WRF Regional
869 Model for the Description of Dust Mineralogy in the Atmosphere, *Atmosphere*, 14, 1615,
870 <https://doi.org/10.3390/atmos14111615>, 2023b.

871 Song, Q., Ginoux, P., Gonçalves Ageitos, M., Miller, R. L., Obiso, V., and Pérez García-Pando, C.:
872 Modeling impacts of dust mineralogy on fast climate response, *Atmospheric Chemistry and*
873 *Physics*, 24, 7421–7446, <https://doi.org/10.5194/acp-24-7421-2024>, 2024.

874 Su, L. and Fung, J. C.: Sensitivities of WRF-Chem to dust emission schemes and land surface properties
875 in simulating dust cycles during springtime over East Asia, *Journal of Geophysical Research:*
876 *Atmospheres*, 120, 11–215, <https://doi.org/10.1002/2015JD023446>, 2015.

877 Tang, W., Yang, K., Qin, J., Li, X., and Niu, X.: A 16-year dataset (2000–2015) of high-resolution (3 h,
878 10 km) global surface solar radiation, *Earth System Science Data*, 11, 1905–1915,
879 <https://doi.org/10.5194/essd-11-1905-2019>, 2019.

880 Tong, D. Q., Gill, T. E., Sprigg, W. A., Van Pelt, R. S., Baklanov, A. A., Barker, B. M., Bell, J. E., Castillo,
881 J., Gassó, S., and Gaston, C. J.: Health and safety effects of airborne soil dust in the Americas
882 and beyond, *Reviews of Geophysics*, 61, e2021RG000763,
883 <https://doi.org/10.1029/2021RG000763>, 2023.

884 Tuccella, P., Menut, L., Briant, R., Deroubaix, A., Khvorostyanov, D., Mailler, S., Siour, G., and
885 Turquety, S.: Implementation of Aerosol-Cloud Interaction within WRF-CHIMERE Online
886 Coupled Model: Evaluation and Investigation of the Indirect Radiative Effect from
887 Anthropogenic Emission Reduction on the Benelux Union, *Atmosphere*, 10, 20,
888 <https://doi.org/10.3390/atmos10010020>, 2019.

889 Usher, C. R., Michel, A. E., and Grassian, V. H.: Reactions on mineral dust, *Chemical reviews*, 103,
890 4883–4940, <https://doi.org/10.1021/cr020657y>, 2003.

891 Wang, X., Zhang, L., and Moran, M. D.: Development of a new semi-empirical parameterization for
892 below-cloud scavenging of size-resolved aerosol particles by both rain and snow, *Geoscientific*
893 *Model Development*, 7, 799–819, <https://doi.org/10.5194/gmd-7-799-2014>, 2014.

894 Willis, P. T. and Tattelman, P.: Drop-size distributions associated with intense rainfall, *Journal of Applied*

895 Meteorology and Climatology, 28, 3–15, <https://doi.org/10.1175/1520->
896 0450(1989)028%253C0003:DSDAWI%253E2.0.CO;2, 1989.

897 Zhang, L., Gong, S., Padro, J., and Barrie, L.: A size-segregated particle dry deposition scheme for an
898 atmospheric aerosol module, Atmospheric environment, 35, 549–560,
899 [https://doi.org/10.1016/S1352-2310\(00\)00326-5](https://doi.org/10.1016/S1352-2310(00)00326-5), 2001.

900 Zuo, X., Zhang, C., Zhang, X., Wang, R., Zhao, J., and Li, W.: Wind tunnel simulation of wind erosion
901 and dust emission processes, and the influences of soil texture, International Soil and Water
902 Conservation Research, 12, 455–466, <https://doi.org/10.1016/j.iswcr.2023.08.005>, 2024.

903
904
905
906